15th IFK
Proc. of the 15th International Fluid Power Conference <Symposium/Conference>
<DOI>

Physics-Informed Neural Network-Based Prediction of Mixed Lubrication Characteristics on Cylinder Block/Valve Plate Interfaces via Mechanism-Data Integration

Dingchong LYU [1], Jian FU [2], Shoujun ZHAO [3]

[1]*Beihang University, by2207123@buaa.edu.cn*

[2]*Beihang University, fujian@buaa.edu.cn*

[3]*Beijing Institute of Precision Mechatronics and Controls, shoujunzhao@vip.sina.com*

Abstract.

Aerospace electro-hydrostatic modules (EHMs) play a critical role in precision actuation for flight control systems. The cylinder block/valve plate (CB/VP) interfaces of EHMs are subject to extreme lubrication failure under high-frequency alternating conditions. Typical failures include fluid starvation caused by the gate effect at ultra-high speeds, as well as accelerated wear resulting from boundary friction spikes during low-speed reversals. These issues pose great challenge to conventional analysis, as the high computational cost and inherent instability of high-fidelity simulations present a critical barrier to developing reliable EHM systems. To address these challenges, this study developed a physics-informed neural network (PINN) framework that integrates physical principles with data-driven deep learning. By conducting experiments on the CB/VP interface thermal characteristics under specified operational conditions, the acquired dataset served as the basis for developing a mapping model that correlates operational parameters (rotational speed and pressure) with interface temperature. This established relationship was subsequently integrated into a mixed lubrication model, yielding a thermo-elasto-hydrodynamic (TEHD) coupling simulation framework incorporated into the PINN architecture. Experimental validation demonstrated that the PINN-based model achieved significantly better agreement with measured outputs compared to conventional theoretical predictions, The implemented deep learning methodology enabled precise prediction of mixed lubrication characteristics, maintaining physical consistency while achieving data-driven accuracy. The proposed PINN framework will be extended to investigate rotor dynamics and vibrational behavior in future studies. This work provides enhanced insights into interfacial lubrication mechanisms and establishes an innovative paradigm for analyzing high-performance aerospace servo systems.

Keywords. electro-hydrostatic actuator, deep learning, thermo-elasto-hydrodynamic coupling, tribo-pair.

1. INTRODUCTION

Aerospace Electro-Hydrostatic Module (EHM) work as the critical power components for precision applications such as thrust-vector control and flight-surface actuation, operate under extreme high-frequency quadrant-altering conditions [1–3]. The integrated EHM architecture induces significant rotor vibrations that critically destabilize the lubrication regime at the cylinder block/valve plate (CB/VP) interface [4,5]. This dynamic environment generates two distinct failure modes unobserved in conventional hydraulic systems. The first is gate effect-induced self-priming suppression: At ultra-high speeds [6], transient flow barriers cause lubricant starvation. While near zero-speed zones, frequent reversals provoke friction spikes that intensify adhesive wear and can lead to catastrophic seizure [7,8]. These phenomena constitute fundamental limitations for achieving reliable lubrication in aerospace EHMs.

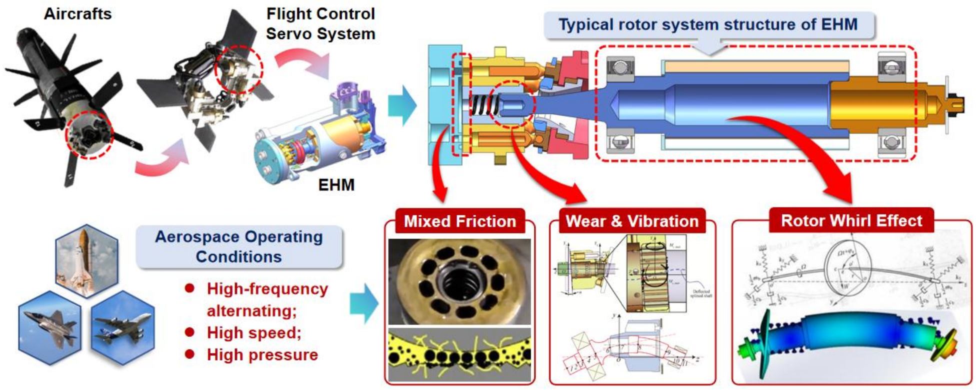

Figure 1.1. Challenges of aerospace highly-compact EHM

Traditional theoretical and numerical methods exhibit significant limitations: high-fidelity models suffer from convergence difficulties [9–12] while predictions consistently deviate from experimental friction torque measurements. System instability has been identified as the root cause [2], and rotor dynamics modelling has revealed critical speed behavior [13]. Although DLC-CrN coatings demonstrate wear resistance [6–8], these methods fail to accurately characterize friction transitions under transient conditions, reflect dynamic oil film rupture/reconstruction processes, or establish wear-vibration coupling frameworks. While artificial neural networks (ANN) show strong function approximation capabilities, purely data-driven approaches face substantial limitations.

To address these challenges, Physics-Informed Neural Networks (PINNs) embed governing equations into neural architectures, achieving synergistic integration of physical principles and data features [14,15]. Faras et al. [16] validated PINNs as effective solvers for elastohydrodynamic lubrication problems, and further demonstrated their versatility in handling both hydrodynamic and EHD regimes [17]. Addressing computational cost, they achieved significant acceleration in contact analysis compared to traditional methods [18]. Moreover, hard-constraint formulations [19] were introduced to strictly enforce physical boundaries, while Ahmed et al. [20] successfully integrated these surrogate models into digital twins for real-time monitoring of lubricated systems. And Yin et al. [21] established a coupled framework resolving cross-scale challenges in seawater-lubricated friction pairs.

This study integrates PINNs into a thermo-elasto-hydrodynamic (TEHD) coupling framework, enabling precise prediction of mixed lubrication characteristics and providing innovative research directions for characterizing complex dynamic behaviors of servo motor pump cylinder block/valve plate pairs under typical power spectra.

To overcome the limitations of conventional methods in analyzing the lubrication performance, this study developed a mechanism-data fused PINN model for the CB/VP interface. The research established a mixed lubrication numerical model, constructed the PINN framework, and validated its predictive accuracy against experimental data. The results demonstrate the efficacy of the proposed data-mechanism integration approach.

2. Mixed Lubrication Numerical Model of CB/VP Interface

To analyze the tribological interface between the CB/VP tribo-pair, mathematical and numerical models are employed to simulate its mixed lubrication regime, characterized by partial fluid film and partial asperity contact. These models serve as traditional tools for performance prediction, design optimization, and service life extension [13,22].

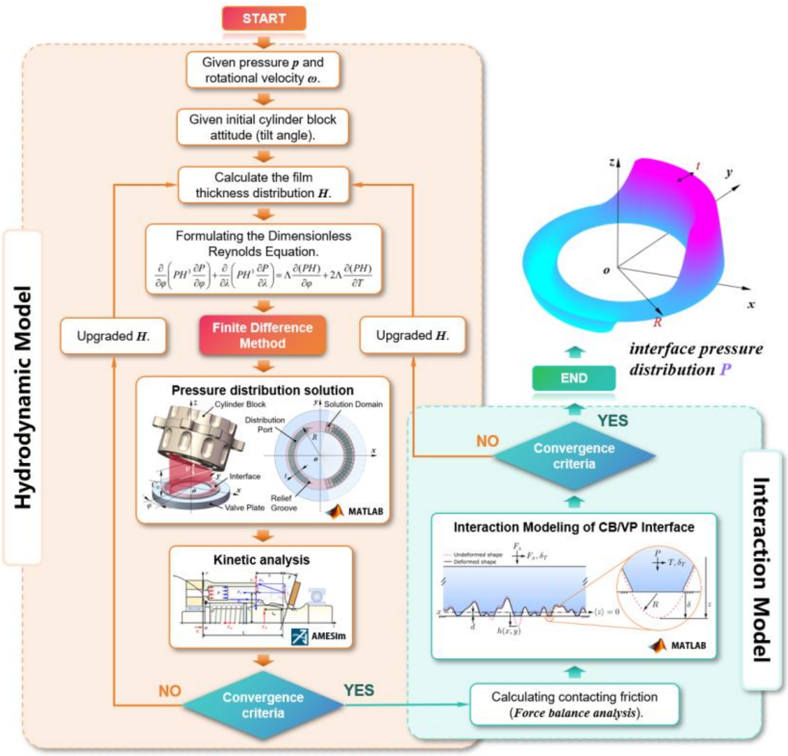

Figure 2.1. Elasto-hydrodynamic numerical modelling framework

2.1. EHD Coupling Modelling Framework

Based on the elasto-hydrodynamic (EHD) model that integrates geometric, lubrication, and contact performance analyses, the procedure for determining the optimal tolerance of the CB/VP interface is structured as follows: Initially, geometric tolerances, including cylindricity error and dimensional deviations of the piston and cylinder, are characterized [9,10,23]. Subsequently, the fluid pressure distribution at the interface is solved by coupling fluid dynamics with the mechanical equilibrium of the cylinder assembly. This pressure distribution is then input into a contact mechanics model (the Greenwood-Williamson contact model, G-W model [24]) to achieve fluid-solid domain coupling. Finally, the resulting film thickness and pressure distributions are used to compute key performance parameters such as friction losses and leakage rates.

a) *Hydrodynamic Model*

The CB/VP interface represents a critical tribo-pair that integrates sealing, bearing, and lubricating functions [6]. As the contact interface with the largest surface area in EHM systems, it serves as the primary site for cavitation, leakage, and wear failures, thereby fundamentally constraining the performance ceiling of the entire system. The dynamically engaged region highlighted in red in Fig. 2.2(a) constitutes the core area of lubrication analysis.

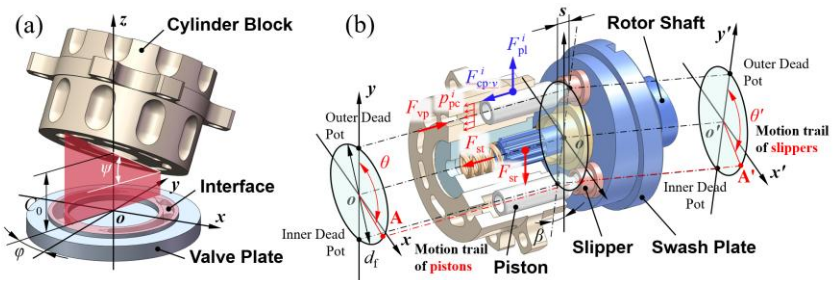

Figure 2.2. Geometric relationship of cylinder block/valve plate interface [22]

To characterize its hydrodynamic behavior, the dimensionless Reynolds equation is employed in this study. The pressure field is normalized using the contact zone's mid-radius (radial direction) and the nominal film thickness (normal direction) as characteristic length scales [13]. This approach ensures numerical stability and eliminates potential errors induced by dimensional inconsistencies during the computational process. Based on this framework, the following equation is established:

$$\frac{\partial}{\partial \varphi}\left(\rho H^3 \frac{\partial P}{\partial \varphi}\right)+\frac{\partial}{\partial \lambda}\left(\rho H^3 \frac{\partial P}{\partial \lambda}\right)=\Lambda \frac{\partial(\rho H)}{\partial \varphi}+2\Lambda \frac{\partial(\rho H)}{\partial T} \quad (2.1)$$

$$\Lambda=\frac{6\mu\omega}{P_a}\left(\frac{R}{C_0}\right)^2 \quad (2.2)$$

Where φ and λ denote the dimensionless circumferential and radial coordinates, respectively. T is the dimensionless operating time. P and H represent the dimensionless oil pressure and oil film thickness, respectively. ρ denotes the density of the hydraulic working medium. Λ denotes the scaling factor, and it is defined by the mid-radius of the interface R, rotational velocity ω, hydraulic medium viscosity η, nominal clearance C_0, and standard atmospheric pressure P_a.

Fig. 2.2(b) depicts the dynamic equilibrium of the cylinder block assembly. A lumped-parameter model representing the integrated cylinder block-piston-slipper-swash plate system was established in AMESim to characterize the multi-body dynamics. Detailed modelling methodology is provided in Ref [25]. And tilting angle ψ of the cylinder block are incorporated into the characterization of H, as can be shown below.

$$H = \frac{C_0 + R\sin\psi\cos(\varphi + \varphi_0)}{R} \tag{2.3}$$

b) *Interaction Model*

The G-W model is a classical theory in contact mechanics, specifically employed to calculate elastic contact between rough surfaces. The core of this model lies in idealizing a rough surface as a series of elastic hemispheres with varying heights, and deriving the overall contact behavior by superposing the contact solutions of individual hemispheres. By quantifying the contact laws governing rough surfaces, this model provides a crucial theoretical framework for subsequent research in the field [24].

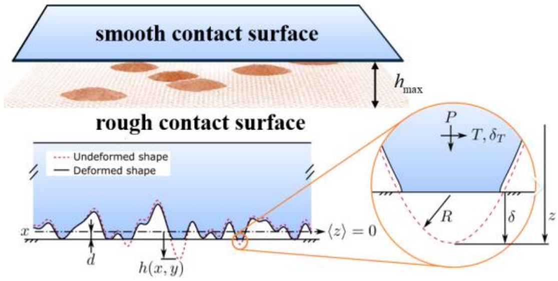

Figure 2.3. The Greenwood-Williamson contact mechanics model [24]

In this model, one of the rough surfaces is assumed to consist of an infinite number of independent hemispheres with identical radii, and the heights of these hemispheres follow a Gaussian distribution. The formula for the probability density function f (h) is given as follows:

$$f(h) = \frac{1}{\sigma\sqrt{2\pi}} exp\left(-\frac{(h-\mu)^2}{2\sigma^2}\right) \tag{2.4}$$

Where h is the height coordinate of an individual asperity, σ is the standard deviation of asperity height distribution, μ is the mean value of asperity height distribution.
Whereas the other surface is assumed to be perfectly smooth. Meanwhile, it is postulated that the contact between each individual hemisphere and the rigid plane is an independent event; the total contact force and contact area are thus the sum of contributions from all hemispheres that come into contact. The formula for the total contact force F is shown as follows:

$$F = \frac{4}{3} E * R^{\frac{1}{2}} n_0 \int_{h_c}^{\infty} (\partial + h - h_c)^{\frac{3}{2}} f(h) \mathrm{d}h \tag{2.5}$$

Where E is the equivalent elastic modulus, R is the equivalent radius of asperities, n_0 is the asperity density, δ is the normal displacement, h_c is the contact threshold height.

2.2. Numerical Solution Methodology

The pressure distribution is solved using a circumferential difference scheme combined with an elliptic partial differential equation iterative configuration. The circumferential difference equations ensure continuity of pressure and film thickness in the annular solution domain, while the elliptic formulation enables rapid convergence of the nonlinear fluid governing equations. This approach facilitates subsequent contact mechanics calculations. For specific implementation details, refer to [13].

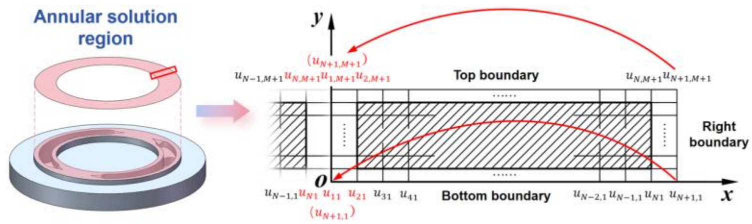

Figure 2.4. Circumferential finite difference discretization of the CB/VP Interface [13]

3. PINN Prediction Model via Mechanism-Data Integration

This study introduces a novel dual-domain nested PINN framework. Its loss function is innovatively constructed by integrating experimental data from EHM characteristic tests with multi-physics governing equations.

3.1. Deep Learning Prediction Framework

A dual-layer nested neural network architecture with mechanism-data fusion is developed in this research. The inner-layer network employs data-driven ANNs, which are trained on thermal characteristic test data from the CB/VP interface to predict its thermal characteristics. The trained ANN model is subsequently embedded to constitute a TEHD model. The outer-layer PINN framework incorporates TEHD governing equations and experimental data into its loss function, enabling accurate prediction of mixed friction characteristics at the CB/VP interface, as shown in Fig 3.1.

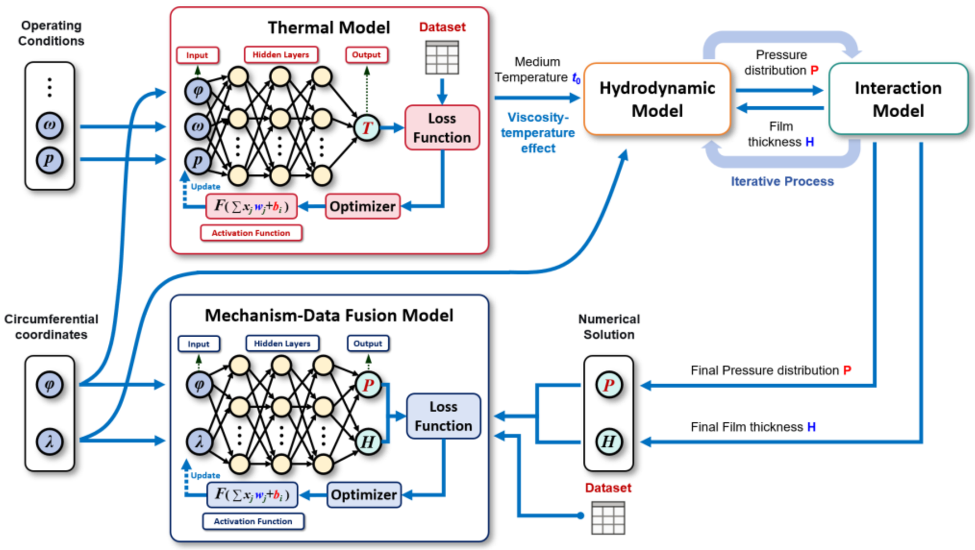

Figure 3.1. Mechanism-data fusion-based PINN prediction framework

Based on the EHD model for the CB/VP pair described in Section 2., where the fluid viscosity μ is initially a constant, an ANN-based temperature prediction model is now nested. Under specified outlet pressure and rotational speed boundary conditions, the ANN first computes the temperature distribution T across the CB/VP interface. This predicted temperature field is subsequently used to determine the spatially varying fluid viscosity μ_d via a temperature-viscosity effect. The updated, non-uniform viscosity field is then fed into the subsequent hydrodynamic and contact mechanics calculations, enabling a fully coupled TEHD simulation. Due to the fast computational speed of the ANN model, the overall computation time of this TEHD model remains comparable to the EHD model.

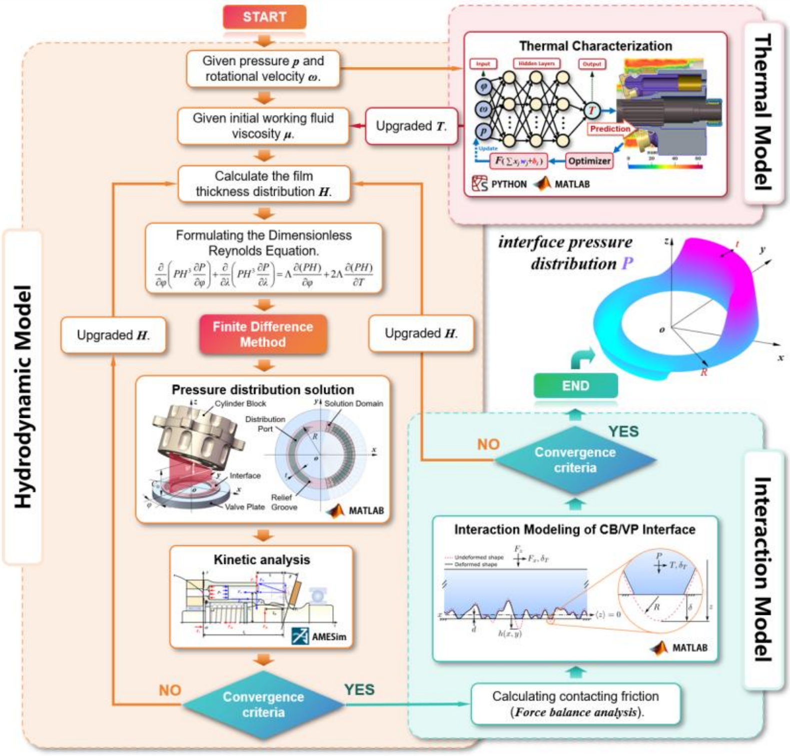

Figure 3.2. Thermal-elasto-hydrodynamic model based on PINN thermal prediction

3.2. Loss Function

The loss functions for the two nested neural networks are respectively defined, broadly categorized into theoretical loss and data loss.

a) Implementation of Mechanism-Data Integration

In the dual-layer nested architecture of this study, the neural networks in both the inner and outer layers share an identical internal structure. The distinction lies solely in the composition of their loss functions and the number of parameters in the input and output layers, as illustrated in Fig 3.3. and Fig 3.4. As depicted in Fig 3.3., the loss function directly computes the difference between the training set values and the predicted outputs, subsequently optimized by adjusting biases and weights through a solver.

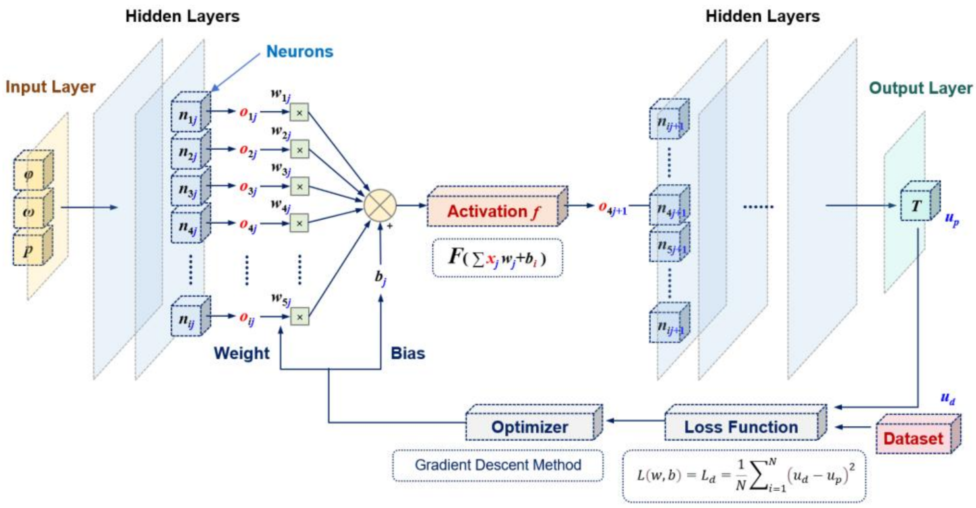

Figure 3.3. Training process of interface thermal prediction

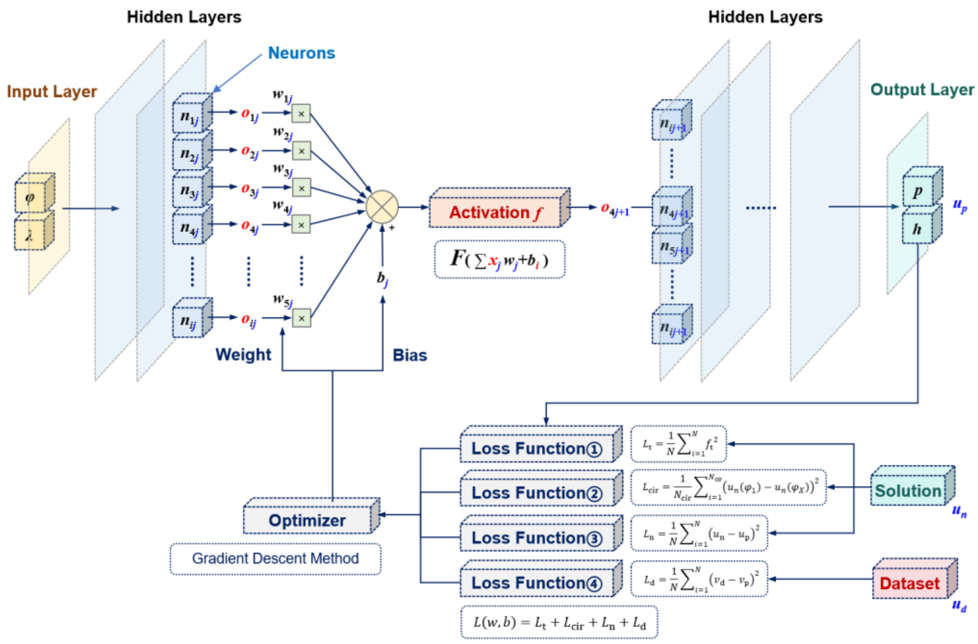

Figure 3.4. Training process of mixed lubrication prediction

In contrast, the loss function in the outer PINN framework shown in Fig 3.4. is considerably more complex. It incorporates the theoretical loss derived from the governing equations and data loss from numerical solutions. A key advantage of PINN architecture lies in its flexibility: unlike traditional equation systems that may suffer from over-constraint issues, the loss components in PINN can be seamlessly integrated without such limitations. However, it is important to note that simply stacking excessive loss terms does not necessarily enhance training accuracy and efficiency.

b) *Theoretical Loss*

In the nested architecture employed in this work, the theoretical error resides solely within the outer PINN framework and arises from the following three distinct sources, where u_{nn} denotes the prediction value. *N* denotes all types of collocation points (interior points set, boundary condition set, and circumferential boundary set):

1) the first component originates from physical equations, constructed by substituting the PINN outputs for dynamic pressure distribution *P* and film thickness distribution *H* into Eq. (2.1) and (2.5), then calculating the mean squared error between the left-hand and right-hand sides of these governing equations.

$$L_{t1} = \frac{1}{N_{in}} \sum_{i=1}^{N_{in}} \left(f_l(u_{nn}) - f_r(u_{nn}) \right)^2 \tag{3.1}$$

2) Second, the boundary condition error encompasses four segments: the inner and outer boundaries of the CB/VP interface, along with both kidney-shaped groove boundaries. The pressure values at the two kidney-shaped grooves are set to the high- and low-pressure zone values respectively, while the interface boundaries are assigned the chamber pressure.

$$L_{t2} = \frac{1}{N_b} \sum_{i=1}^{N_b} \left(u_{nn}(\varphi_{b1}, \lambda_{b1}) - P_b \right)^2 \tag{3.2}$$

3) Third, the circumferential continuity error arises from the annular solution domain of the CB/VP interface as mentioned in Section 2.2. This requires the nodal values, first-order partial derivatives, and second-order partial derivatives at the left and right boundaries of the nodal matrix to be consistent, ensuring periodicity across the computational domain.

$$L_{t2} = \frac{1}{N_c} \sum_{i=1}^{N_c} \left(u_{nn}(\varphi_{b1}, :) - u_{nn}(\varphi_{br}, :) \right)^2 \tag{3.3}$$

$$L_{t2}' = \frac{1}{N_c} \sum_{i=1}^{N_c} \left(\frac{\partial u_{nn}(\varphi_{b1}, :)}{\partial \varphi} - \frac{\partial u_{nn}(\varphi_{br}, :)}{\partial \varphi} \right)^2 \tag{3.4}$$

$$L_{t2}'' = \frac{1}{N_c} \sum_{i=1}^{N_c} \left(\frac{\partial^2 u_{nn}(\varphi_{b1}, :)}{\partial \varphi \partial \lambda} - \frac{\partial^2 u_{nn}(\varphi_{br}, :)}{\partial \varphi \partial \lambda} \right)^2 \tag{3.5}$$

c) *Data Loss*

Under this nested architecture, the two neural networks exhibit distinct data loss: 1) The data for the inner ANN model is entirely derived from EHM thermal tests, with its training set constructed from measured data. 2) The two output quantities of the outer PINN model (dynamic pressure distribution *P* and film thickness distribution *H*) have no direct correlation with temperature parameters. Consequently, measured temperature data cannot be directly used to build its training set. Instead, numerical solutions obtained from the TEHD model embedded with the ANN are employed as training data, which integrates thermal test data with mechanistic modelling. Nevertheless, both neural networks adopt identical loss function expressions, as shown below:

$$L_d = \frac{1}{N_t} \sum_{i=1}^{N_t} \left(u_{nn} - u_d \right)^2 \tag{3.6}$$

where u_d denotes the data value at a specific collocation point. *Nt* denotes all collocation points. The term L_d directly computes the mean squared error between the deep learning predicted values and the data values across all collocation points in the training set.

3.3. Network Training Configuration

Hyperparameter selection for neural networks remains predominantly experience-dependent, as these choices critically govern the model's convergence behavior, predictive accuracy, and computational overhead [14].

a) Network Architecture

Based on established research [26], the mesh configurations for the dual nested networks have been defined and are presented in Table 3.1. Notably, the ANN training set comprises 10 Operating Points (OPs) × 5 Measuring Points (MPs), whereas the PINN training set is constituted by 20% of the available numerical solution nodes.

Table 3.1. Parameter settings for network training

Networks	Hidden layers	Neurons	Training set size
1) Thermal prediction ANNs	4	20	10 OPs × 5 MPs = 50
2) Lubrication prediction PINNs	4	50	20% of numerical nodes

b) Activation Function and Optimizer

The Multilayer Perceptron (MLP) is constructed with 'Tanh' activation functions and trained using the 'Adam' optimizer, minimizing a mean squared error (MSE) loss that integrates numerical data with governing equations.

4. EXPERIMENTAL VALIDATION

This section details the experimental rig's modular architecture. A multi-level temperature monitoring system with distributed armoured thermocouples at the CB/VP interface enables automated data acquisition. The collected dataset is used to develop a PINN prediction model.

4.1. Overall Performance Test Platform of EHM

The experimental platform comprises three main modules. The first module is a high-frequency variable-condition motor-pump load simulation module, integrating a load simulation system, external control system for simulated loads, oil replenishment system for the tested servo pump, circulation filtration system, cooling system, residual oil recovery system, and hydraulic signal acquisition module. The second module is a human-machine interaction interface consisting of quick-connect components, safety monitoring systems, and display/control panels. The third module is an electronic control multi-dimensional real-time perception system incorporating signal acquisition and control units, with the physical setup shown in Fig 4.1.

Through coordinated operation of its modular systems, the platform performs essential functions including basic parameter testing, load simulation, system pressurization, oil temperature control, and data storage. A multi-level temperature monitoring system was established on the CB/VP interface using armored thermocouples. As shown in Fig. 4.2, a set of sensors were circumferentially arranged near the valve plate and embedded through radial drilling. The thermal testing module can automatically acquire temperature signals in real time and stored them in a database for the PINN training process.

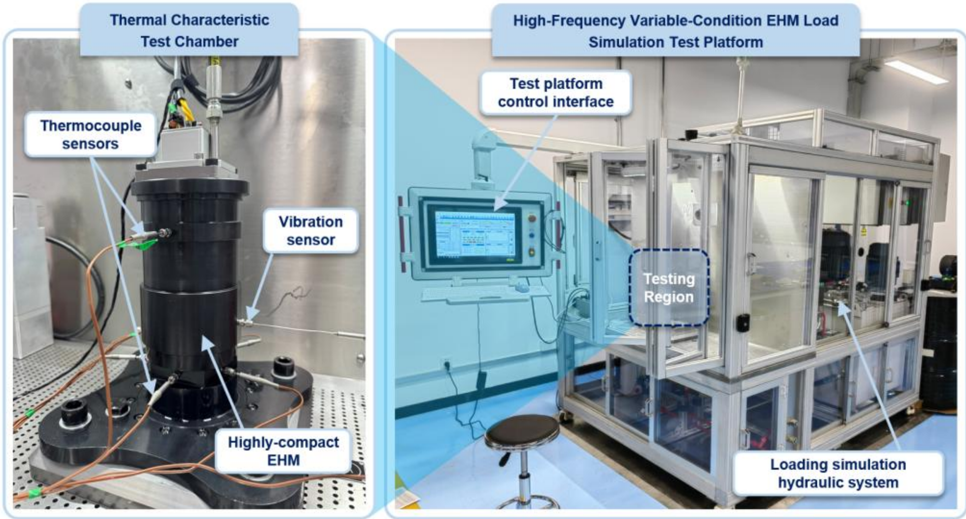

Figure 4.1. The overall performance test platform of EHM

4.2. Dataset Acquisition: Thermal Characteristic Test of CB/VP Interface

The dataset was constructed through the following three-step procedure: 1) First, temperature data were collected from all monitoring points during operation from initial startup to steady-state conditions at each designated working point. 2) Next, a mapping array was constructed using rotational speed ω, outlet pressure P, and initial temperature T_0 as inputs, with the corresponding steady-state temperatures as outputs. 3) And then, neural network architecture described in Section 3.2 was employed to train a temperature prediction model for the CB/VP interface using the developed dataset. 4) At last, the PINN prediction model of thermal characteristics was integrated into the TEHD framework. The curves shown in Fig 4.2. were measured under constant conditions of 14 MPa and 4000 r/min.

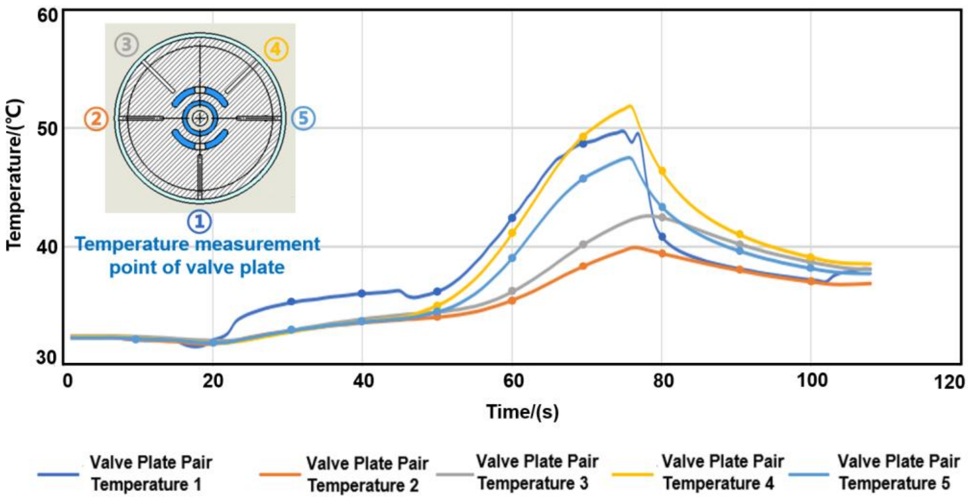

Figure 4.2. Thermal characteristic testing of EHM

5. Results And Discussion

Model accuracy was assessed by comparing experimental data with EHD and PINN simulations. The influence of training epochs was then systematically analyzed to validate the model's precision. Ultimately, the PINN prediction on lubrication was finished.

5.1. Prediction Accuracy Comparison

As depicted in Figure 5.1, the leakage data and predictions are compared with experimental measurements across four operating points. The vertical axes denote the output pressure and rotational speed (represented by blue and red polylines), and the horizontal axis lists the operating points. The actual leakage, along with the predictions from both models, are visualized using bar clusters, with respective values detailed in Table 5.1.

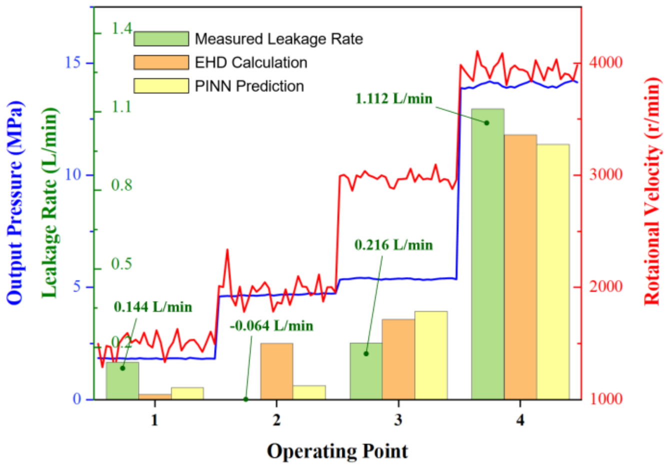

Figure 5.1. Comparisons of measured and predicted leakage rates

A comparative analysis of the relative errors shows a vastly wider distribution for the EHD model (13.9% to 332.8%) than for the PINN model (32.5% to 156.6%). The EHD model showed significant deviations, especially at Operating Points 2 and 3, whereas the PINN model yielded lower errors at all points except one. The significantly lower mean error of the PINN model confirms its superiority, indicating not only higher average precision but also better adaptability to different operating conditions and enhanced robustness.

Table 5.1. Operating point setting and leakage values

Operating Conditions	**Operating Points**			
	I	**II**	**III**	**IV**
Outlet Pressure (MPa)	1.842	4.679	5.390	14.03
Rotational Velocity (r/min)	1496	1968	2972	3938
Measured Leakage (L/min)	0.1438	-0.06440	0.2161	1.112
EHD Calculation (L/min)	0.02004	0.2143	0.3068	1.012
PINN Prediction (L/min)	0.04677	0.05293	0.3383	0.9748

The PINN model's training progress was analyzed by tracking its predictive accuracy across epochs. Detailed outputs, including numerical results and contour plots, were examined at eight key nodes. As shown in Fig. 5.2, the prediction error converged significantly from 1596.1% to 4.08%. This improvement was not entirely uniform, as a noticeable error rebound occurred at 40000 iterations.

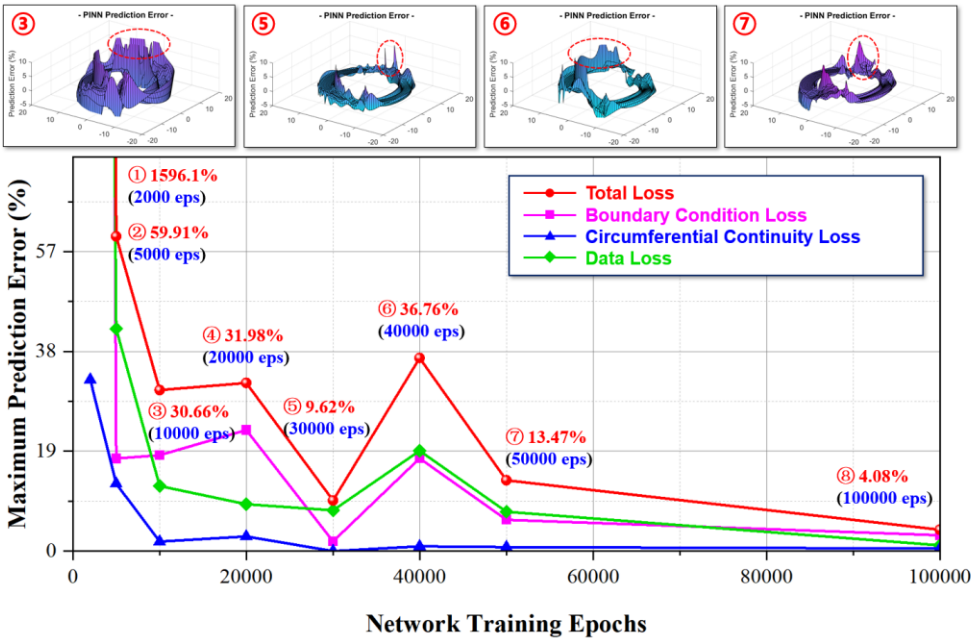

Figure 5.2. PINN prediction accuracy across various training epochs

By comparing the boundary loss, data loss, and circumferential continuity loss separately, it can be further observed that across different training epochs, the locations of maximum error consistently lie on the inner and outer boundaries of the solution domain, rather than at circumferential discontinuities. The influence of circumferential continuity loss is minimal, with errors being primarily driven by boundary loss and data loss. As the number of training epochs increases, the boundary loss shows a clear oscillatory decline, while the data loss fluctuates more irregularly. Additionally, errors near the two dead zones are larger than in other regions, with the locations of maximum error predominantly concentrated in these areas.

5.2. Mechanism-Data Fusion-Driven Prediction of Lubrication Characteristics

The PINN model demonstrates a decisive computational advantage by performing complete simulations and generating detailed contour plots within milliseconds. This stands in stark contrast to the conventional EHD model, which requires approximately 10 minutes to solve due to its inherent computational bottlenecks, a limitation that is further exacerbated by longer solve times and convergence challenges in its more complex TEHD formulation. The remarkable efficiency of the PINN approach enabled the extensive simulation of the interface's mixed lubrication state across a wide spectrum of operating conditions, as comprehensively detailed in Figure 5.3.

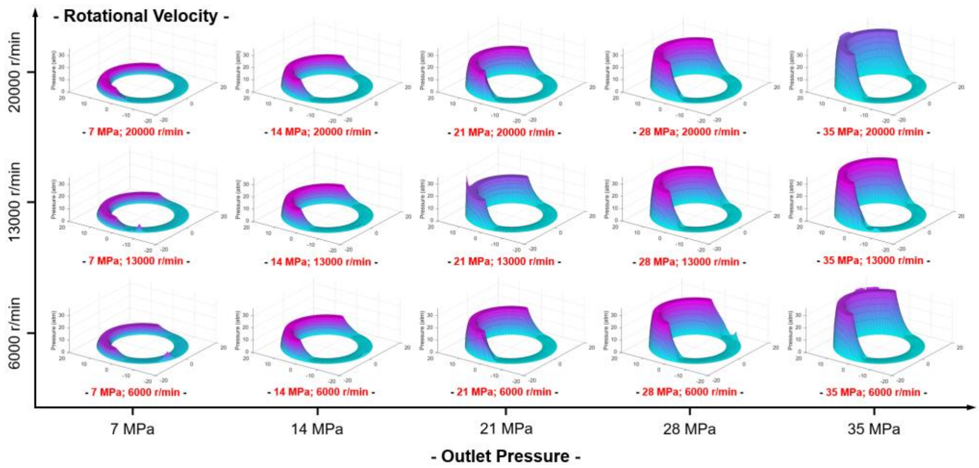

Figure 5.3. PINN prediction of mixed lubrication under various operating conditions

The pronounced growth of oil film thickness in the high-pressure zone under increasing load, at a constant speed, underscores the critical role of pressure in governing film formation. Meanwhile, variations in rotational velocity under a constant pressure condition exhibit minimal impact on the pressure profiles within critical areas such as the dead zone and kidney port, thereby maintaining the overall pressure landscape largely unchanged. Furthermore, the inherent operational tilt of the cylinder block is confirmed to generate an asymmetric oil film distribution, which sporadically triggers intense local pressure concentrations, manifesting as isolated, sharply defined peaks within the contour plots.

6. CONCLUSION

This study pioneers a mechanism-data fused PINN prediction method for analyzing the lubrication regime in aerospace EHM's CB/VP interface. The framework synergizes thermal experiments with EHD modelling, achieving unprecedented predictive accuracy over conventional methods. It significantly enhances the prediction accuracy and efficiency of mixed lubrication parameters while rigorously preserving physical consistency. The principal findings include:

- The PINN model demonstrates superior predictive accuracy over the conventional EHD approach, with a substantially narrower relative error range (32.5%-156.6% vs 13.9%-332.8%) and significantly lower mean error across four operating conditions.
- Training iterations critically influence model convergence, reducing prediction error from 1596.1% to 4.08%. The temporary error resurgence at 40,000 iterations represents a natural optimization phenomenon, while the overall downward trend confirms the value of extended training. Meanwhile, PINN enables millisecond-level simulations versus 10 minutes for EHD.
- The key lubrication mechanisms are revealed: pressure-dominated film formation, minimal speed impact on pressure profiles, and tilt-induced asymmetric film distribution with localized pressure peaks.

7. REFERENCES

[1] J.-C. Maré, J. Fu, ‘Review on Signal-by-Wire and Power-by-Wire Actuation for More Electric Aircraft’, Chin. J. Aeronaut., 30(3), pp. 857–870, 2017. doi: 10.1016/j.cja.2017.03.013.

[2] D. Lyu, et. al., ‘Key Technologies and Challenges of High-Performance Servo Motor Pump’, Acta Aeronaut. Astronaut. Sin., 45(15), p. 630225, 2024. doi: 10.7527/S1000-6893.2024.30225.

[3] J. Zhao, et. al., ‘Review of Cylinder Block/Valve Plate Interface in Axial Piston Pumps: Theoretical Models, Experimental Investigations, and Optimal Design’, Chin. J. Aeronaut., 34(1), pp. 111–134, 2021. doi: 10.1016/j.cja.2020.09.030.

[4] Y. Fu, et. al., ‘Electrohydraulic Pump Development Status and Key Technology Review’, Mach. Tool Hydraul., 40(1), pp. 143–149, 2012.

[5] S. Zhao, et. al., ‘The Study on the Dynamic Capability of an Electro-Hydrostatic Actuator to Drive a Large Inertia Load’, Proc. of the IEEE/ASME International Conference on Advanced Intelligent Mechatronics (AIM), pp. 836–841, 2016. doi: 10.1109/aus.2016.7748169.

[6] J. Zhao, et. al., ‘Experimental Research on Tribological Characteristics of TiAlN Coated Valve Plate in Electro-Hydrostatic Actuator Pumps’, Tribol. Int., 155, p. 106782, 2021. doi: 10.1016/j.triboint.2020.106782.

[7] J. Fu, et. al., ‘Tribological Characteristics of Hard-to-Hard Matching Materials of Cylinder Block/Valve Plate Interface in Electro-Hydrostatic Actuator Pumps’, Proc. Inst. Mech. Eng. Part C J. Mech. Eng. Sci., 237(14), pp. 3320–3333, 2023. doi: 10.1177/09544062231189692

[8] D. Lyu, et. al., ‘Experimental Research on Friction Characteristics of DLC Coated Cylinder Block/Valve Plate Interface in Aerospace Integrated Motor Pumps’, 2023 Asia-Pacific International Symposium on Aerospace Technology (APISAT 2023) Proceedings, pp. 1141–1156, 2024. doi: 10.1007/978-981-97-4010-9-89.

[9] H. Deng, et. al., ‘Lubrication Characteristics of Valve Plate Pair of Balanced Large Flow Pump Based on Elastic Deformation’, Flow Meas. Instrum., 95, p. 102514, 2024. doi: 10.1016/j.flowmeasinst.2023.102514.

[10] Y. Lu, et. al., ‘Comparative Study on Asymmetric and Symmetric Configurations of Valve Plates in Axial Piston Pumps’, Proc. of the ASME/BATH Symposium on Fluid Power and Motion Control (FPMC), p. V001T01A056, 2024. doi: 10.1115/fpmc2024-140112.

[11] R. Chacon, M. Ivantysynova, ‘Advanced Virtual Prototyping of Axial Piston Machines’, Proc. of the 9th FPNI Ph.D. Symposium on Fluid Power, p. V001T01A026, 2016. doi: 10.1115/fpni2016-1561.

[12] L. Shang, M. Ivantysynova, ‘An Investigation of Design Parameters Influencing the Fluid Film Behavior in Scaled Cylinder Block/Valve Plate Interface’, Proc. of the 9th FPNI Ph.D. Symposium on Fluid Power, p. V001T01A027, 2016. doi: 10.1115/fpni2016-1540.

[13] D. Lyu, et. al., ‘Development of Boundary/Mixed Friction Models for Cylinder Block/Valve Plate Interface in a Novel Aerospace Electro-Hydrostatic Module’, Proc. of the ASME/BATH Symposium on Fluid Power and Motion Control (FPMC), p. V001T01A057, 2024. doi: 10.1115/fpmc2024-140246.

[14] H. Gao, et. al., ‘Physics-Informed Neural Network for Solving Hydrodynamic Lubrication Characteristics of Piston Pump Slipper Pair’, Tribol. Int., 181, p. 108290, 2025. doi: 10.13052/rp-9788743808251a11.

[15] X. Deng, et. al., ‘Fast Prediction of Flow Field in Scramjet Combustor Based on Physical Information Neural Network under Wide Mach Number’, Chin. J. Aeronaut., 38(7), p. 103482, 2025. doi: 10.1016/j.cja.2025.103482.

[16] F. Brumand-Poor, et. al., ‘Physics-Informed Neural Networks as Solvers for Elastohydrodynamic Lubrication Problems’, Proc. 13th Int. Fluid Power Conf. (IFK), 2022.

[17] F. Brumand-Poor, et. al., ‘Extrapolation of Hydrodynamic Pressure in Lubricated Contacts: A Novel Multi-Case Physics-Informed Neural Network Framework’, Lubricants, 12(4), p. 122, 2024. doi: 10.3390/lubricants12040122.

[18] F. Brumand-Poor, et. al., ‘Fast Computation of Lubricated Contacts: A Physics-Informed Deep Learning Approach’, Proc. 14th Int. Fluid Power Conf. (IFK), 2024.

[19] F. Brumand-Poor, et. al., ‘Physics-Informed Neural Networks for the Reynolds Equation with Transient Cavitation Modeling’, Lubricants, 2(11), p. 365, 2024. doi: 10.3390/lubricants12110365.

[20] A. Saleh, et. al., ‘Real-Time Prediction of Pressure and Film Height Distribution in Plain Bearings Using Physics-Informed Neural Networks (PINNs)’, Lubricants, 13(8), 360, 2025. doi: 10.3390/lubricants13080360.

[21] F. Yin, et. al., ‘Physics-Informed Machine Learning for Tribological Propertie s Prediction of S32750/CFRPEEK Tribopair under Seawater Lubrication via PISSA-CNN-LSTM’, Tribol. Int., 199, p. 109965, 2024. doi: 10.1016/j.triboin t.2024.109965.

[22] D. Lyu, et. al., ‘Investigations on Thermal-Fluid Coupling Characteristics of an Innovative Compact Electro-Hydrostatic Module (EHM) Considering Rotor Churning Effects’, Proc. of the 17th International Symposium on Fluid Power, pp. 1–10, 2024.

[23] B. Han, et. al., ‘Analysis of Friction Characteristics of Valve Plate Pair in an Axial Piston Pump Considering Cylinder Block Dynamics’, J. Tribol., 146(4), p. 041702, 2024. doi: 10.1115/1.4064116.

[24] Y. Xu, et. al., ‘An Asperity-Based Statistical Model for the Adhesive Friction of Elastic Nominally Flat Rough Contact Interfaces’, J. Mech. Phys. Solids, 164, p. 104878, 2022. doi: 10.1016/j.jmps.2022.104878.

[25] J. Zhao, et. al., ‘Flow Characteristics of Integrated Motor-Pump Assembly with Phosphate Ester Medium for Aerospace Electro-Hydrostatic Actuators’, Chin. J. Aeronaut., 35(12), pp. 256–271, 2022. doi: 10.1016/j.cja.2022.11.013.

[26] D. Lyu, et. al., ‘Extreme Variable-Speed Lubrication Dynamics of Cylinder Block/Valve Plate Interface Based on Neural Network Method’, Proc. of the 2025 Swedish International Conference on Fluid Power (SICFP2025), 2025. doi: 10.13052/rp-9788743808251a24.

Biographies

Lyu Dingchong received the bachelor's degree in mechanical engineering from Wuhan University of Technology in 2019, the master's degree in mechanical engineering from Xi'an Jiaotong University in 2022, respectively. He is currently pursuing the philosophy of doctorate degree in mechatronic engineering at the Laboratory of Aerospace Servo Actuation and Transmission, Beihang University. His research focuses on the dynamic and static characteristics of high-performance servo power components and their optimization design theories. He has contributed to multiple national-level research initiatives and has regularly presented his findings at international academic conferences.